Vesicle deformation and poration under strong dc electric fields

Mohamed M. Sadik, Jianbo Li, Jerry W. Shan, David I. Shreiber, and Hao Lin

Vesicle deformation and poration under strong DC electric fields

Mohamed M. Sadik,[1] Jianbo Li,[1] Jerry W. Shan,[1] David I. Shreiber,[2] and Hao Lin[1*]

[1]Department of Mechanical and Aerospace Engineering

[2]Department of Biomedical Engineering

Rutgers, The State University of New Jersey, 98 Brett Rd, Piscataway, NJ 08854, USA

Abstract When subject to applied electric pulses, a lipid membrane exhibits complex responses including electrodeformation and electroporation. In this work, the electrodeformation of giant unilamellar vesicles under strong DC electric fields was investigated. Specifically, the degree of deformation was quantified as a function of the applied field strength, and the electrical conductivity ratio of the fluids inside and outside of the vesicles. The vesicles were made from L-α-phosphatidylcholine with diameters ranging from 14 to 30 μm. Experiments were performed with the field strength ranging from 0.9 to 2.0 kV/cm, and the intra-to-extra-vesicular conductivity ratio varying between 1.92 and 53.0. With these parametric configurations, the vesicles exhibited prolate elongations along the direction of the electric field. The degree of deformation was in general significant. In some cases, the aspect ratio of a deformed vesicle exceeded 10, representing a strong-deformation regime previously not explored. The aspect ratio scaled quadratically with the field strength, and increased asymptotically to a maximum value at high conductivity ratios. Appreciable area and volumetric changes were observed both during and after pulsation, indicating the concurrence of electroporation. A theoretical model is developed to predict these large deformations in the strongly-permeabilized limit, and the results

---

[*]Corresponding author; Email: hlin@jove.rutgers.edu

are compared with the experimental data. Both agreements and discrepancies are found, and the model limitations and possible extensions are discussed.

I. INTRODUCTION

The application of electric pulses to cells or vesicles induces complex responses. The lipid membrane may become porated, which is a phenomenon known as electroporation. It may also deform under electromechanical and electrohydrodynamic forces, which is a phenomenon known as electrodeformation. Electroporation is widely employed in both biological research and clinical applications, in areas including drug and gene delivery, protein insertion, cancer therapy, and other processes where access to the cytoplasm is desired [1-4]. Electrodeformation, on the other hand, can be harnessed as a means to probe membrane properties [5, 6], and to detect pathological changes in cells [7]. Electroporation has been extensively studied for over three decades with well-developed modeling and diagnostic tools [8-15]. In contrast, electrodeformation received more attention during the past decade. Although research in this area began much earlier [5, 16-19], a significant body of data only became available in the recent years with the development of high-performance optical imaging systems [20-28].

Electrodeformation may occur with both AC and DC electric fields. When investigating this phenomenon, most authors used vesicles as a model system (instead of biological cells) due to their relative simplicity and controllability. An AC field in general induces a variety of relatively stationary deformations based on the frequency domain. For this reason, it is used to systematically quantify membrane responses, often in the absence of membrane poration. Helfrich and co-authors, for instance, analyzed area changes of deformed vesicles to infer the bending rigidity of the membrane [5, 6]. Dimova and co-authors performed extensive studies to

2

characterize vesicle morphological types (prolate, oblate, and spherical) in the parametric space of field frequency and intra-to-extra-vesicular conductivity ratio [20, 23]. These studies were later complemented with an electrohydrodynamic theory by Vlahovska *et al.* to interpret the observed trends and regimes [28]. Electrodeformation under DC fields, on the other hand, is transient and dynamic. Due to the high field strength normally used in these DC studies, membrane poration often occurs concurrently. In a series of work, Neumann and co-authors studied the electroporative deformation of vesicles hundreds of nanometers in size [24]. At this range, direct optical observation is difficult, and alternative techniques such as conductometrical and turbidimetrical measurements were employed. The data were analyzed to extract useful information such as pore statistics, vesicle volumetric reduction, and the correlation between membrane curvature and pore formation. In contrast, direct observation of giant vesicles (typically a few tens of microns in diameter) under the action of a field can reveal rich and complex details of the dynamic process. In [26], Riske and Dimova developed a high-speed imaging system to investigate the deformation-relaxation of vesicles under DC electric fields. The results were discussed in relation with the electrotension (the Maxwell stress) on the membrane, as well as various time scales (the viscous relaxation and the pore relaxation), which are important in understanding the membrane relaxation mechanisms post-pulsation. In a companion work, the same authors observed transient, cylindrical deformations when the vesicles were suspended in a salt solution [27].

In this work, the electrodeformation of giant lipid vesicles under strong DC electric fields is investigated with direct optical observation. Unilamellar vesicles 14-30 microns in diameter were formed from L-α-phosphatidylcholine [29], with prescribed intra-to-extra-vesicular conductivity ratios ranging from 1.92-53.0. Direct-current pulses 500 μs in duration and 0.9-

2.0 kV/cm in strength were applied to the suspended vesicles. This arrangement led to strong prolate deformations in which the vesicles elongated along the direction of the applied field. The vesicles were visualized using sucrose-glucose contrast imaging. The deformation was quantified by measuring the aspect ratio of the deformed vesicles, and the changes in the apparent surface area and volume are analyzed both during and after pulsation. The materials and methods are introduced in Sec. II.

Previous work primarily investigated the time course of deformation (in DC fields, [26, 27]), and characterized the various morphological types and the transition from one to another (in both AC and DC fields, [20, 23, 27, 28]). Herein, we focus on one particular morphological type, namely, the prolate deformation under DC electric pulses. We systematically quantify deformation as a function of the controlling parameters, i.e., the field strength, and the intra-to-extracellular conductivity ratio. In contrast to the moderate-deformation regimes (with aspect ratios not exceeding 3) studied before [26, 27], this work extends into a strong-deformation regime. In some conditions, the combination of high field strength and conductivity ratio results in an aspect ratio exceeding 10. Electrodeformation of this magnitude has not been previously reported. Meanwhile, appreciable changes in vesicle surface area and volume are also present, which is consistent with observations by Portet *et al.* [30]. These changes indicate the concurrence of electroporation. The phenomena examined in this work therefore represent a complex new domain where strong, nonlinear deformation is coupled with significant poration of the membrane. The experimental results are presented in Sec. III.

The wide range of data provided by this work is valuable for validating and advancing current understanding, in particular through simultaneous model development. In Sec. IV, we pursue a predictive theory to interpret the experimental results. Our model directly extends from

that by Hyuga *et al.* [17].   In contrast to all previous theories which are limited to the linear, small-deformation regime [5, 16-18, 28], the current model is able to predict large membrane electrodeformations. The model results are compared with the experimental data, which reveals both agreement and discrepancies. In particular, the agreement suggests the dominating role of the electrostatic force in driving the deformation. The discrepancies, on the other hand, point to model limitations. These limitations are discussed together with suggestions for improvements before we draw conclusions in Sec. V.

II.   MATERIALS AND METHODS

A. Preparation of Vesicles

Unilamellar vesicles were formed using an electroformation technique developed by Angelova and Dimitrov [29]. L-α-phosphatidylcholine (from egg-PC, Sigma, St. Louis, MO) was dissolved at an approximate concentration of 2 mg/mL in a pre-mixed chloroform/methanol (9:1, v:v) solution. Three drops of the lipid solution (5 μL each) were deposited on an indium-tin-oxide (ITO) glass slide, which was subsequently dried in a vacuum chamber to remove traces of the organic solvents. A 2.5-mm thick PDMS spacer with a rectangular open space in the middle was placed on the lipid-coated slide, and covered by another ITO slide to form the electroformation chamber. The layered structure was integrated into a resin frame for sealing and handling. Sucrose and sodium chloride (NaCl) were dissolved in de-ionized (DI) water at defined concentrations (discussed below), and the solution was injected into the sealed chamber. An AC electric field, 2 V/mm (RMS) in amplitude and 10 Hz in frequency, was applied through the conductive ITO slides for 40 minutes. A population of vesicles ranging from 14-30 μm in diameter formed due to this process.

The vesicles were aspirated gently from the chamber. The vesicle-liquid mixture was filtered with a syringe filter to remove most of the liquid. The remaining portion was then washed and re-suspended in DI water containing a desired glucose concentration, which generated a difference in the intra-vesicular (sucrose) and extra-vesicular (glucose) solutions. (The solution within the vesicle is assumed to have the same properties as those of the liquid in the electroformation chamber.) This sugar asymmetry allowed imaging of the vesicle due to the contrast in the index of refraction inside and outside of the vesicle [26, 27]. In addition, the electrical conductivities were controlled by altering the NaCl concentration in the intra- and extra-vesicular solutions to probe the effects of this variable on the characteristics of vesicle deformation. The intra-vesicular conductivity ranged from 6.20 $\mu S / cm$ (with no added salt) to 138 $\mu S / cm$ (with 1 mM NaCl). Other conductivities between these values were achieved by increasing the salt concentration gradually. The conductivity of the glucose solution suspending the vesicles ranged from 2.60 $\mu S / cm$ to 3.44 $\mu S / cm$. All conductivity values (Table I) were measured with a conductivity meter (CON 6, Oakton Instruments, Vernon Hills, IL). The osmolalities of the intra- and extra-vesicular solutions were also carefully measured (3D3 Osmometer, Advanced Instruments, Norwood, MA), and matched by moderating the glucose concentration in the extra-vesicular solution to avoid effects due to osmotic pressure.

TABLE I. The intra-to-extra-vesicular conductivity ratio (γ) was varied by controlling the conductivity inside (λ_{in}) and outside (λ_{out}) of the vesicles.

γ	λ_{in} ($\mu S / cm$)	λ_{out} ($\mu S / cm$)
1.92	6.20	3.23
5.97	18.7	3.13
32.6	112	3.44
46.9	138	2.94
53.0	138	2.60

B. Vesicle Electrodeformation/Electroporation and Imaging

To perform electrodeformation studies, approximately 70 μL of vesicle-containing solution was placed in a separate chamber consisting of two stainless steel electrodes ($D = 0.61$ mm) affixed to a microscope slide with a separation distance of 2.75 mm. An electroporator was custom-built to deliver calibrated, controllable, square pulses 300-5000 μs in duration and 0-700 V in amplitude. (Note: By our specific design, the voltage amplitude and pulse shape *did not* depend on the conductivity of the vesicle-containing solution.) The electroporator was synchronized with an imaging system through a timing box (Model 535 Delay Generator, Berkeley Nucleonics, San Rafael, CA). The imaging system consisted of a digital camera (Hamamatsu C4742-95, Bridgewater, USA) connected to an inverted microscope (Olympus IX81, Center Valley, PA). The integrated system allowed the recording of a single image at a defined delay time after the electric pulse started.

The vesicles were visualized using phase-contrast microscopy. For each experiment, three snapshots of an isolated vesicle were acquired. 1) A reference image was taken before the application of an electric pulse to capture the original (spherical) shape and size of the vesicle. 2) After the application of a DC electric pulse, a second image was taken at a defined delay time (with respect to the start-time of the pulse), using the synchronization scheme described above. This image captured the deformed vesicle toward the end of the electric pulse. 3) A final image of the same vesicle was taken a few seconds post-pulsation. The delay was sufficient for the vesicle to relax back to a spherical shape, but with possible membrane loss and size reduction in some cases (see Figs. 1 and 2). All images were post-analyzed using NIH ImageJ.

III. EXPERIMENTAL RESULTS

In a DC electric field, the morphological type of a deformed vesicle is controlled by its intra-to-extracellular conductivity ratio [23, 26, 27], which we henceforth denote by γ. For example, $\gamma > 1$ induces a prolate deformation where the vesicle elongates along the direction of the applied field, whereas $\gamma < 1$ induces an oblate deformation where the vesicle is compressed along the field vector. These behaviors can be explained by the fact that different γ configurations lead to different directions of the electrostatic force on the membrane [22].

In this work, we focus on the prolate regime ($\gamma > 1$). Vesicles were prepared with five intra-to-extra-vesicular conductivity ratios as described above, namely, $\gamma = 1.92$, 5.97, 32.6, 46.9, and 53.0 (Table I). For each conductivity ratio, three electric field strengths were applied, $E = 0.9$, 1.5, and 2.0 kV/cm, all with a 500 μs pulse duration. For the second image, the delay time was set to be 350 μs. The camera exposure time was 150 μs. This arrangement ensured that the second image (see Fig. 1(b) and Fig. 2(b)) captured the averaged vesicle dynamics during the last 150 μs of the electric-field pulse (between 350-500 μs after pulse initialization).

A series of electrodeformation experiments, 85 in total, were performed. Representative deformations and recoveries are shown in Figs. 1 and 2. Fig. 1(a) shows a pre-pulsation vesicle, with an initial radius (denoted by D_i) of 25.9 μm. The conductivity ratio was $\gamma = 53.0$. Fig. 1(b) shows the same vesicle at the end of an electric pulse, with the direction oriented from right to left, and a magnitude of 0.9 kV/cm. The geometric shape was well-fitted with an ellipse (black dotted line). An aspect ratio, p, defined as the ratio of the major and minor axes of the fitted ellipse, is used to quantify the degree of deformation (Fig. 1(b)). For the case shown in
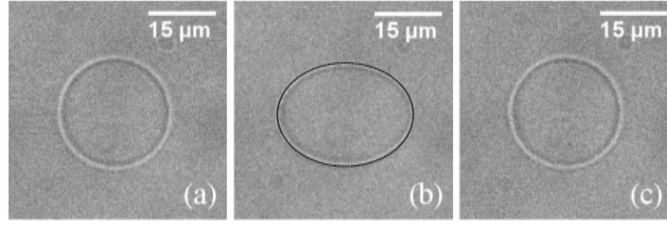
FIG. 1. Bright-field images of a vesicle before (a), during (b), and after (c) the application of an electric pulse. The vesicle was originally $D_i = 25.9$ μm in diameter. The applied field was $E = 0.9$ kV/cm and pointing from right to left. The conductivity ratio was $\gamma = 53.0$. The shape of the vesicle during application of the electric field is fitted with an ellipse (black dotted line) using ImageJ (b). The vesicle demonstrated a moderate prolate deformation with an aspect ratio of $p = 1.31$. No obvious size reduction is shown in the post-pulsation image (c).

Fig. 1(b), $p = 1.31$. As seen in Fig. 1(c), the vesicle relaxed back to a spherical shape approximately 2 seconds post-pulsation. The diameters before and after pulsation are obtained by similarly fitting the vesicle images with circles (not shown). No apparent membrane loss or size reduction was observed in the case shown in Fig. 1.

In contrast, Fig. 2 shows a stronger deformation during the electric pulse (Fig. 2(b)), and an appreciable shrinkage after the pulse is switched off (Fig. 2(c)). The initial diameter was $D_i = 28.8$ μm, the conductivity ratio was $\gamma = 46.9$, and the electric field strength was 1.5 kV/cm (also pointing from right to left). Although the polar caps are not clearly visible for the deformed vesicle in Fig. 2(b), possibly due to a loss of membrane, or a temporary loss of the sucrose/glucose contrast in the proximity of the poles induced by membrane permeabilization,[†] the shape is still well-fitted with an ellipse ($p = 3.57$). We emphasize that in this and other similar cases, the vesicles may have local irregularities (especially toward the polar areas) causing deviations from ellipsoidal shapes. The fitted ellipse is therefore an *estimate* of the realistic vesicle geometry. However, we believe that such a fitting is a reasonable

---

[†] Membrane permeabilization allows an exchange of solution across, resulting in a temporary reduction in the sugar contrast. However, the exchange did not completely equilibrate the solutions. Fig. 2(c) shows that sufficient contrast evidently remained for membrane visualization.
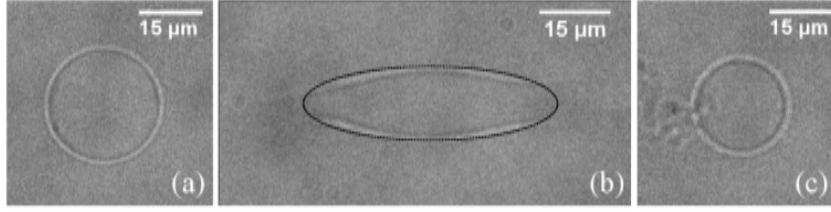
9

FIG. 2. Bright-field images of a vesicle before (a), during (b), and after (c) the application of an electric pulse. The vesicle was originally $D_i = 28.8$ μm in diameter. The applied field was $E = 1.5$ kV/cm and pointing from right to left. The conductivity ratio was $\gamma = 46.9$. The shape of the vesicle during application of the electric field is fitted with an ellipse (black dotted line) using ImageJ (b). The vesicle demonstrated a large prolate deformation with an aspect ratio of $p = 3.57$. The polar caps are not clearly visible in (b), possibly due to membrane poration. The post-pulsation image (c) shows an appreciable reduction in vesicle size.

approximation. Similar situations occur, e.g., in [26] (see Fig. 5 therein), where it can be more clearly seen that although the polar boundaries become fuzzy and less visible, the proper vesicle is still in general ellipsoidal. Alternatively, we have attempted to obtain contour fitting of the vesicles without any presumption on their shape (not shown). When compared with results from elliptical fitting, this more direct and precise approach reveals differences of around 1% for the aspect ratio, and 2-4% for surface area and volume (examined in Fig. 4 below). We therefore opt to adopt the elliptical fitting method based on its simplicity and in consideration of the large amount of data involved. In Fig. 2(c), the post-pulsation image shows obvious size reduction when compared with Fig. 2(a). The membrane loss was possibly caused by one of the three mechanisms discussed by Portet *et al.* [30].

The quantitative results of the experiments are summarized in Figs. 3-5. In Fig. 3, the aspect ratio, p, of the deformed vesicles is plotted against the initial vesicle diameter, D_i, for the three field strengths studied. Different geometrical symbols represent different γ values. At the relatively low field strength ($E = 0.9$ kV/cm), the deformation aspect ratio is around 2 for all conductivity ratios, as seen in Fig. 3(a). As the field strength is increased to 1.5 kV/cm (Fig.
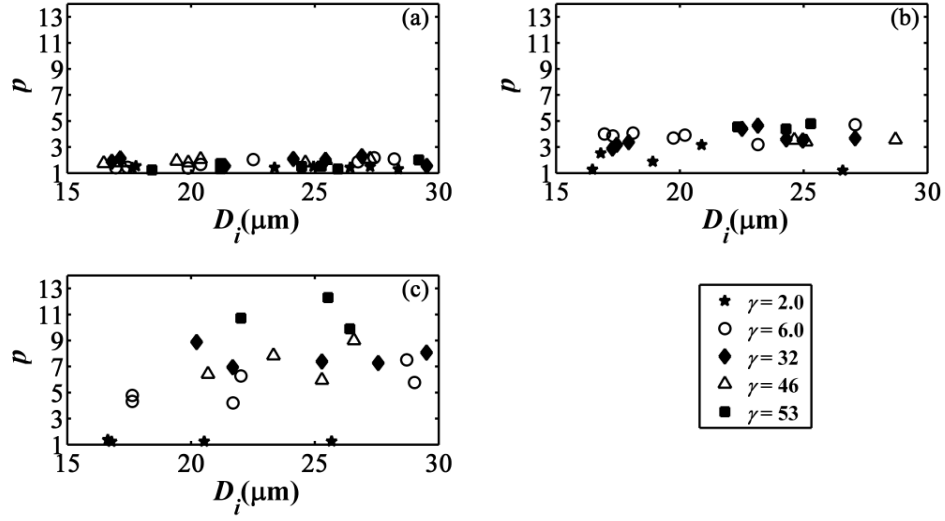
10

FIG. 3. The aspect ratio of deformed vesicles (p) induced by three electric fields strengths: (a) 0.9 kV/cm, (b) 1.5 kV/cm, and (c) 2.0 kV/cm. The pulse width was 500 μs for all the experiments. Each data point represents a single experiment. The values for p are obtained from analyzing images in the same manner as in Figs. 1(b) and 2(b).

3(b)), higher deformation aspect ratios (exceeding 4) are observed, and are accompanied by a more obvious dependence on γ. At the highest field strength ($E = 2.0$ kV/cm), very large deformations with values of p approaching 13 are present, in particular at the highest conductivity ratio, $\gamma = 53.0$. For all cases studied, no obvious dependence of p on D_i is observed. A more detailed analysis of the dependence of the deformation ratio on the field strength and the conductivity ratio will be presented in Fig. 5 below.

Associated with the morphological changes, the vesicles also underwent dynamic changes in the apparent surface area and volume. The changes are analyzed by the following formulae:

$$\alpha_d = \frac{(A_d - A_i) \times 100}{A_i}, \qquad \varpi_d = \frac{(V_d - V_i) \times 100}{V_i}, \qquad (1)$$

$$\alpha_f = \frac{(A_f - A_i) \times 100}{A_i}, \qquad \varpi_f = \frac{(V_f - V_i) \times 100}{V_i}. \qquad (2)$$

11

Here α and ϖ denote the relative percentage change in the apparent surface area (A) and volume (V) of each vesicle, and the subscripts i, d, f denote "initial", "during", and "final", respectively. All of A_i, A_f and V_i, V_f are calculated assuming the vesicle is spherical, and the radius is estimated from a fitting on images similar to Fig. 1(a),(c) and Fig. 2(a),(c) (showing the initial and final stages of the vesicle). A_d and V_d are calculated to capture the changes during field-application, also from a fitting of the images. As we previously mentioned, the vesicle is assumed to be an ellipsoid and is axisymmetric with respect to the direction of the applied field.

Fig. 4(a) and (b) demonstrate that vesicle deformation during an applied electric field is associated with surface-area dilation ($\alpha_d > 0$) and volume reduction ($\varpi_d < 0$). In the figure, cyan, red, and black denote the field strengths of 0.9, 1.5, and 2.0 kV/cm, respectively. Different symbols represent different conductivity ratios. Both the surface area and volume vary approximately linearly with respect to the deformation ratio, p. Based on the data, the surface area increases with increasing field strength and conductivity ratio. However, this increase in surface area is accompanied by a volume reduction. These trends provide strong indication of membrane poration. When a spherical vesicle becomes ellipsoidal, and assuming that the volume does not initially change, the surface area has to increase, possibly via both the unfolding of the excess area and elastic stretching of the membrane [19, 26]. Further deformation beyond the compensation of these mechanisms can only occur via leaking of the (incompressible) fluid contained, namely, by means of electroporation. Volume reduction is therefore a natural consequence of large deformations observed in the current experiments. An increase in the apparent area, A_d, on the other hand, is speculated to be a combination of the unfolding effects of the excess area, the presence of pores, and the thinning and structure rearrangements of the membrane [19, 31].
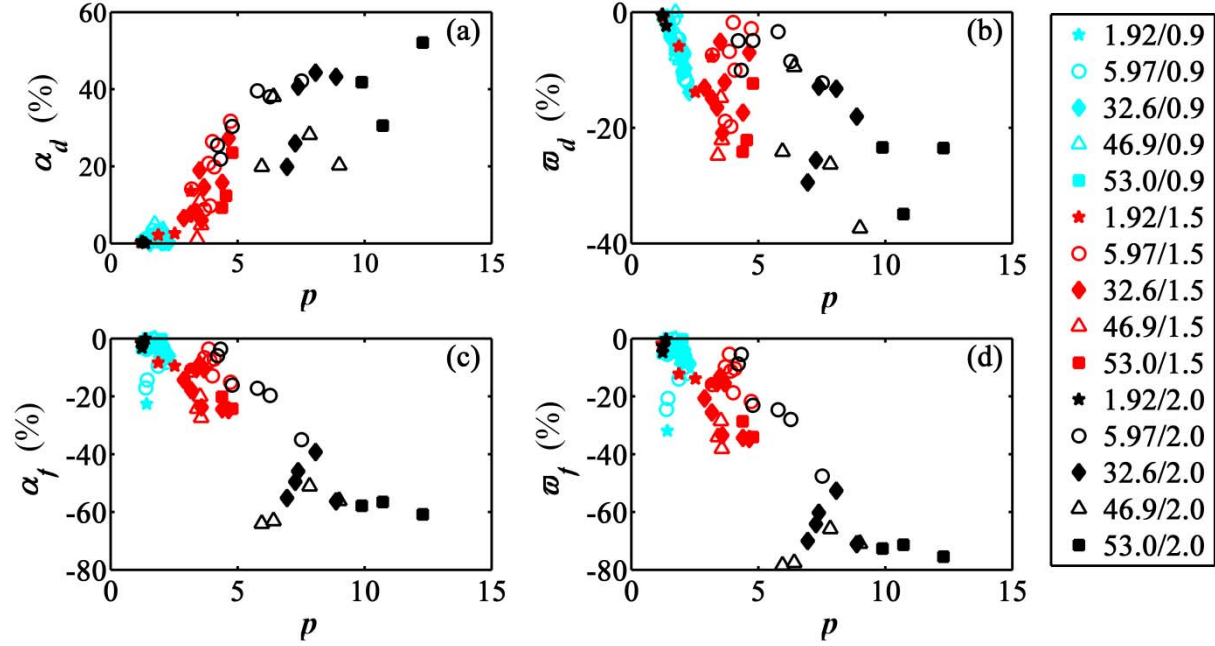
FIG. 4. (Color online) Percentage change in the apparent membrane surface area (α) and vesicle volume (ϖ) during (subscript d) and after (subscript f) pulsation, and as a function of the aspect ratio, p. In the legend, the numbers (e.g., 1.92/0.9) denote combinations of γ / E, with E in units of kV/cm. The surface area increases during pulsation and then decreases after the pulse is ceased. The volume decreases consistently throughout the process.

Fig. 4(c) and (d) show the concurrence of area and volumetric reduction (α_d, $\varpi_d < 0$)

after the vesicles recovered to the final, spherical shape post-pulsation. The correlations of α_d

and ϖ_d with p are similarly monotonic, with some vesicles losing up to 60% of surface area

and almost 70% of volume. For the case presented in Fig. 2, the membrane surface area loss was

27%, and the volume reduction was 37% by our calculation. When compared with Fig. 4(b),

Fig. 4(d) demonstrates further volume reduction during the recovery process. This observation

confirms that pore-sealing was not immediate after the field was switched-off, and further fluid

leakage occurred during this phase. The results corroborate well with those by Portet *et al.* [30],

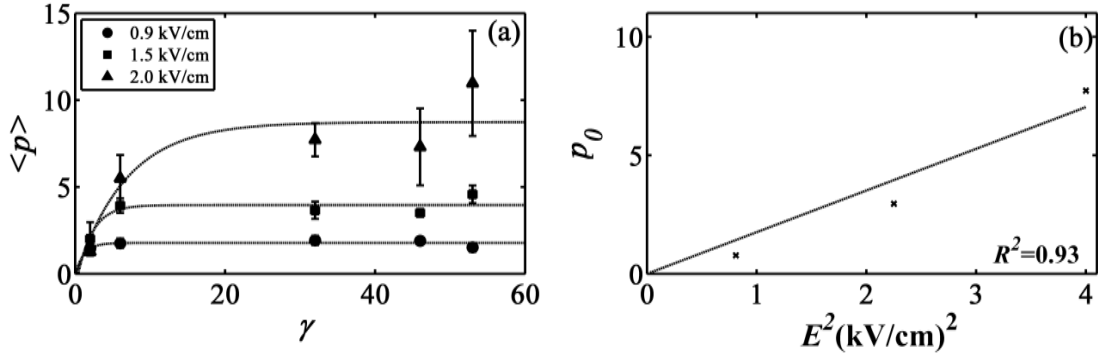which proposes that membrane loss is induced by the formation of (small) vesicles, tubules,

FIG. 5. (a) The average aspect ratio, $\langle p \rangle$, as a function of the conductivity ratio, γ. The error bar represents the standard deviation of each subset. The parameters for the exponential fits (Eqn. (3), dashed) are listed in Table II. (b) The fitted constant p_0 exhibits a linear scaling with E^2. The dashed line is a least-square linear fit, $p_0 = 1.76E^2$. The coefficient of determination is $R^2 = 0.93$.

and/or pores. (However, note that in [30], a similar degree of loss is achieved with multiple pulses, not a single pulse as in the present study.)

In Fig. 5(a), the systematic dependence of the deformation ratio on the conductivity ratio, γ, and the field strength, E, is examined. Here we define an average deformation ratio, $\langle p \rangle$, which is calculated by taking the average of all values of p in each subset of vesicles with identical conductivity ratio and field strength. The error bars indicate standard deviation. The deformation ratio has a positive correlation with the electric field, which has been indicated by Fig. 3. The dependence of $\langle p \rangle$ on γ shows a rapid rise followed by a relative plateau. The data is fitted with an exponential function of the form,

$$\langle p \rangle = p_0 \left(1 - e^{\frac{1-\gamma}{\gamma_p}} \right) + 1 \tag{3}$$

which is shown as dashed lines in Fig. 5(a). The fitting parameters p_0 and γ_p for each data set are given in Table II. Importantly, the constant p_0 exhibits a quadratic scaling with E (Fig.

TABLE II. Constants from the exponentially fitted data using Eqn. (3). The fitted curves are shown in Fig. 5(a).

E (kV/cm)	p_0	γ_p
0.9	0.78	1.20
1.5	2.96	2.02
2.0	7.73	6.72

5(b)), indicating the dominant role of the Maxwell stress in driving the deformations. In the next section, we attempt to develop a model to quantitatively predict the measurements.

IV.   THEORY

The phenomenon studied in this work represents a regime where the complex physics of electrodeformation and electroporation are highly coupled. A comprehensive model including all detailed physical processes, namely, permeabilization, fluid motion and leakage, and large deformation is currently not available. Specifically, all existing theories are limited to the linear regime where the deformation is assumed to be small, and cannot be applied to the case studied in this work [16-18, 28, 32]. Here we pursue a predictive model for large deformations by directly extending from previous work by Hyuga *et al.* [17], where the authors studied the effects of a permeabilized, conducting membrane, in contrast to others who consider deformation in the non-permeabilized regime. Hence their framework is more appropriate for the current case. In the theory described below, we adopt the same physical principles as outlined by Hyuga *et al.* [17] to derive the equation of motion for the deforming membrane. However, instead of solving the problem in the linearized, small-deformation regime using spherical harmonics, we adopt a rotational spheroidal coordinate system to allow for the prediction of arbitrarily large aspect ratios.

Our primary assumption is that the vesicle remains ellipsoidal in shape, thereby ignoring all other shape modes. This approximation follows from our data analysis in Sec. III, and is supported by many experimental observations [16, 20, 23, 26-28]. A similar treatment for large electrodeformations of droplets is found, for example, in Bentenitis and Krause [33]. For this case, the rotational spheroidal coordinate system is suitable to describe the geometry. The coordinates (ξ, η) are related to a cylindrical system (ρ, z) as

$$\begin{cases} z = c\xi\eta, \\ \rho = \sqrt{x^2 + y^2} = c\sqrt{(\xi^2 - 1)(1 - \eta^2)}. \end{cases} \tag{4}$$

Here z and ρ denote the axial and radial coordinates, respectively, c is a constant, and is taken to be $c = \sqrt{a^2 - b^2}$ for an ellipsoid with axes a and b ($a > b$). In this system, the surface of the ellipsoid is conveniently given as

$$\xi = \xi_0 \equiv a / c = a / \sqrt{a^2 - b^2}. \tag{5}$$

For the derivation below, we also define a shape factor, Θ, which is related to ξ_0 and the aspect ratio ($p = a / b$) as

$$p = 1/\cos(\Theta), \quad \xi_0 = 1/\sin(\Theta). \tag{6}$$

Following Hyuga *et al.* [17], we further assume that the total vesicle surface area, *S*, is conserved:

$$S = \int_{-1}^{1} 2\pi ab[1 - (c^2 / a^2)\eta^2]^{1/2} d\eta = 4\pi a_0^2, \tag{7}$$

where a_0 is the radius of the un-deformed, spherical vesicle. We subsequently obtain

$$a = a_0 \sqrt{\frac{2\tan\Theta}{\sin(\Theta)\cos(\Theta) + \Theta}}, \quad b = a_0 \sqrt{\frac{2\sin\Theta\cos\Theta}{\sin(\Theta)\cos(\Theta) + \Theta}}. \tag{8}$$

Under the constraint (7) and the ellipsoidal assumption, the vesicle geometry is completely characterized by a single parameter, Θ. We emphasize that the surface area conservation is an idealizing assumption to make the model tractable. Further improvement of the model needs to consider area expansion as indicated by Fig. 4.

For the electrical problem, we assume that the Ohmic current is conserved, and that the membrane is permeabilized and conductive:

$$\nabla \cdot \lambda_{in} \nabla \phi_{in} = \nabla \cdot \lambda_{out} \nabla \phi_{out} = 0, \tag{9}$$

$$\mathbf{n} \cdot \lambda_{in} \nabla \phi_{in} = \mathbf{n} \cdot \lambda_{out} \nabla \phi_{out}, \quad \mathbf{t} \cdot \nabla \phi_{in} = \mathbf{t} \cdot \nabla \phi_{out}, \quad \text{at the membrane,} \tag{10}$$

where ϕ is the electric potential, and $\mathbf{t}$ and $\mathbf{n}$ denote the unit tangential and normal vector on the membrane, respectively. Eqns. (9, 10) can be solved in a spheroidal coordinate system. The result pertinent to the current work is the normal component of the Maxwell stress, F_n:

$$F_n = \mathbf{n} \cdot (\mathbf{T}^{out} - \mathbf{T}^{in}) \cdot \mathbf{n}, \quad \mathbf{T} = \varepsilon \left(\mathbf{EE} - \frac{1}{2} |\mathbf{E}|^2 \mathbf{I} \right), \tag{11}$$

where $\mathbf{T}$ is the Maxwell stress tensor, $\mathbf{E}$ is the local electric field vector, $\mathbf{I}$ is a unit tensor, and ε is the permittivity of water. A straightforward calculation reveals

$$F_n = \frac{\varepsilon}{2} E^2 B^2 \left[(\xi_0^2 - 1)(\gamma^2 - 1)\left(\frac{\eta^2}{\xi_0^2 - \eta^2} \right) \right], \tag{12}$$

$$B = \frac{Q_1(\xi_0) - \xi_0 Q_1'(\xi_0)}{\gamma Q_1(\xi_0) - \xi_0 Q_1'(\xi_0)}, \tag{13}$$

where E is the strength of the applied field, Q_1 is a Legendre function of the second kind and order one, and Q_1' denotes its derivative.

The equation of motion follows a Lagrange formulation:

$$\frac{d}{dt}\left(\frac{\partial L}{\partial \dot{\Theta}}\right) - \frac{\partial L}{\partial \Theta}$$

$$= \int (F_n + F_\mu)\left(-\frac{c}{\sin^2 \Theta}\sqrt{1-\eta^2 \sin^2 \Theta} + a_0 \frac{\Theta(2\cos^2 \Theta + 1) + \cos \Theta \sin \Theta}{\sqrt{(2\sin \Theta \cos \Theta(\cos \Theta \sin \Theta + \Theta)^3 (1-\eta^2 \sin^2 \Theta)}}\right)dS. \tag{14}$$

Here $L = K-V$ is a Lagrangian function, where V is the curvature-elastic energy, K is the effective kinetic energy, F_n is the normal component of the electrostatic force defined above, F_μ is an effective viscous force, and the factors in the parenthesis on the right-hand-side represent a virtual displacement with respect to the single independent variable, Θ. The evaluation of each individual term is introduced below.

The curvature-elastic energy, V, is given by the formula:

$$V = \frac{\kappa}{2}\int (H - H_0)^2 dS, \tag{15}$$

where κ is the curvature-elastic modulus, H is the mean curvature, and H_0 is its equilibrium value. For a lipid bilayer membrane, we set $H_0 = 0$. Under the current coordinate system, the curvature is given as

$$H = \frac{\cos^2 \Theta + 1 - \eta^2 \sin^2 \Theta}{(1-\eta^2 \sin^2 \Theta)^{3/2} b}, \tag{16}$$

and the integrated energy is evaluated to be

$$V = \frac{\kappa a \pi}{3 b \sin \Theta}(14\cos \Theta \sin \Theta + 6\Theta + 4\cos^3 \Theta \sin \Theta). \tag{17}$$

The effective kinetic energy, K, and the effective viscous force, F_μ, are calculated with an empirical model, also following Hyuga *et al.* [17],

$$K = \frac{1}{2}\int \rho_m v_n^2 dS, \quad F_\mu = -\mu v_n. \tag{18}$$

Table III. List of model parameters.

Symbol	Value	Definition
ρ_m	8.63×10^{-3} g/cm^2	Effective mass density [17]
a_0	11.3 μm	Initial vesicle radius
μ	44.3 g/cm^{2}s	Effective viscous coefficient
ε	7.17×10^{-10} F/m	Permittivity of water
κ	5×10^{-20} J	Curvature-elastic modulus [17, 28]
t_p	500 μs	Pulse length

Here ρ_m is an effective mass density (per unit area of the membrane), μ is an effective viscous coefficient, and v_n is the normal component of the velocity for a point on the deforming membrane:

$$v_n = \frac{b\sin\Theta\,\eta^2 + b'\cos\Theta}{\sqrt{1-\eta^2\sin^2\Theta}\,\cos(\Theta)}\,\dot\Theta. \tag{19}$$

Here a prime denotes a derivative with respect to Θ, and an over-dot denotes a derivate with respect to time. The details of this empirical model are found in [17].

Finally, substituting Eqns. (12), (17), (18) into Eqn. (14), we obtain the equation of motion in terms of Θ:

$$2K_0\ddot\Theta + K_0'\dot\Theta^2 + V' - Q_\mu\dot\Theta - Q_F = 0. \tag{20}$$

Here K_0, Q_μ, and Q_F are all functions of Θ, and their expressions are given in the Appendix. In Eqn. (20), the first two terms represent the effects due to inertia; the third arises from the membrane elastic response; and the last two are due to the viscous and the electrostatic forces, respectively. Eqn. (20) is solved numerically using parameters listed in Table III, and for the various γ and E values studied in the experiments. For each case, the value for Θ at the end of a 500-μs pulse (the length used in the measurements) is obtained, and the value for p is subsequently calculated using Eqn. (6).

The general dependence of p on γ and E is well-predicted by the model. The results are compared with the experimental data in Fig. 6(a), which reveals good agreement. In the model, we set $a_0 = 11.30\,\mu m$, which is the average radius of the vesicle population we studied in the experiments. The trends can be explained by an analysis of the electrostatic force, F_n. From Eqn. (12), the quadratic dependence of F_n on the applied field strength, E, is evident (see also Fig. 5(b)). In addition, the force scales with the conductivity ratio as

$$F_n \sim \frac{\gamma^2 - 1}{[\gamma Q_1(\xi_0) - \xi_0 Q_1'(\xi_0)]^2}. \tag{21}$$

For small values of γ, and temporarily treating both $Q_1(\xi_0)$ and $\xi_0 Q_1'(\xi_0)$ as constants, Eqn. (21) is simplified to

$$F_n \sim (\gamma^2 - 1)\big/ [\xi_0 Q_1'(\xi_0)]^2. \tag{22}$$

This quadratic relationship explains the initial rapid rise in p with respect to γ. For large values of γ, Eqn. (21) converges to a constant, which explains the plateaus observed in Fig. 5(a). Despite the agreement shown in Fig. 6(a), the model can appreciate further improvement, through the development of a more rigorous framework to predict the physical processes
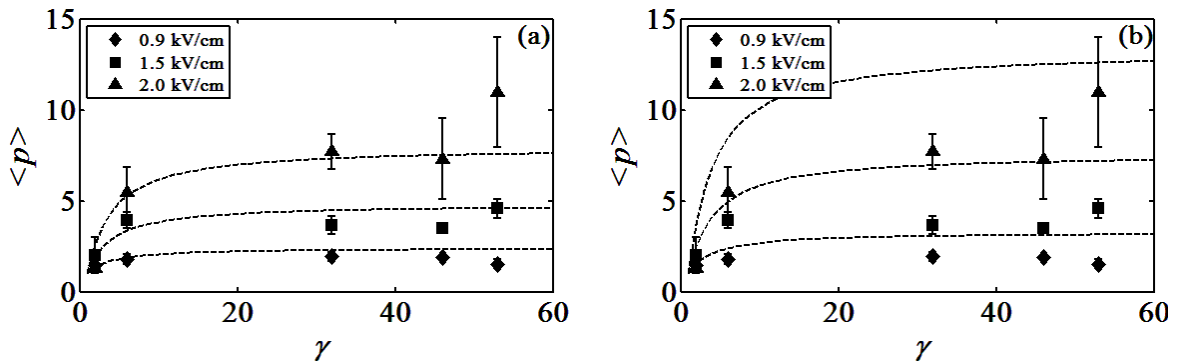

FIG. 6. A comparison between theoretical prediction (dashed) and experimental data (symbols). The data are the same as those in Fig. 5(a). The model results are generated with $a_0 = 11.30$ μm, (a) $\mu = 44.3$ g/cm^{2}s, and (b) $\mu = 22.5$ g/cm^{2}s.

involved. A main limitation of the current theory is that the hydrodynamic problem is treated empirically, with a free parameter, the effective viscous coefficient, μ (Eqn. (18)). In fact, if we decrease the value for μ to the largest value used by Hyuga *et al.* [17] (22.5 g/cm²s), the model overpredicts the deformation ratios (Fig. 6(b)). In addition, there is a discrepancy concerning the dependence of the aspect ratio on vesicle size. Fig. 7 shows the deformation ratio as a function of the initial diameter, D_i. In contrast to the data in Fig. 3, where no obvious dependence on D_i is observed, the model predicts that p decreases with an increasing D_i. This is because in Eqn. (20) the coefficients K_0 (representing the effects of inertia) and Q_μ (representing the viscous effects) scale as a_0^4, where $a_0 = D_i / 2$, whereas the coefficient Q_F (representing the driving electrostatic force) scales as a_0^3. Therefore, as a_0 decreases, the deformation force becomes
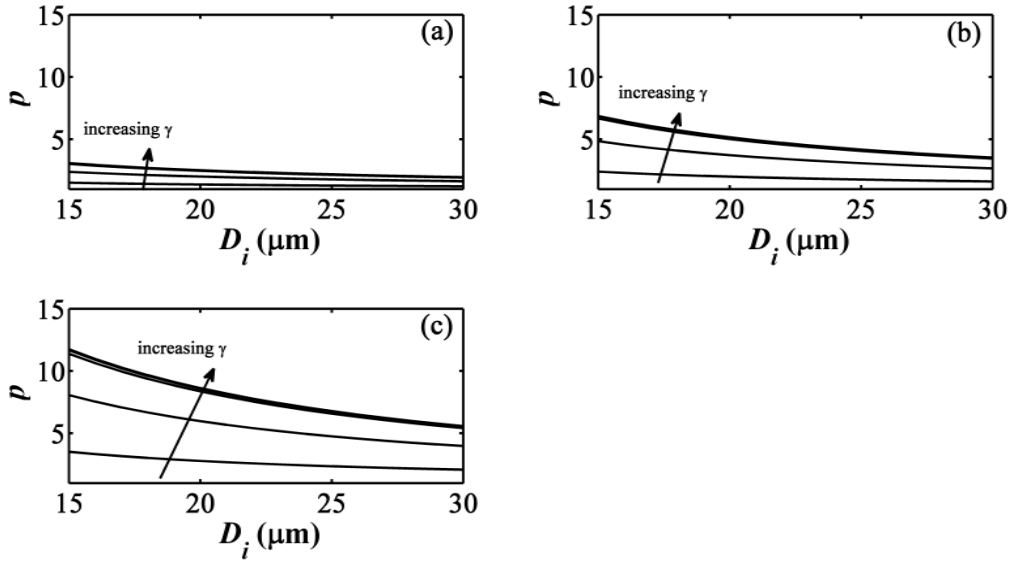

FIG. 7. Predicted aspect ratio, p, as a function of the initial diameter, D_i. The γ values correspond to those used in experiments (Table I). In each graph, the curves for γ = 32.6, 46.9, 53.0 follow each other closely. Contrary to the experimental data in Fig. 3, the aspect ratio has a noticeable dependence on the initial vesicle diameter, D_i.

more dominant relative to the resisting forces. We speculate that this effect is likewise caused by the lack of rigor in calculating the hydrodynamic forces.

We believe that the fidelity of the model may be improved by solving the Stokes equation for fluid motion, also under the rotational elliptical coordinate system, such as to compute the fluid stress on the membrane in a rigorous manner. This task is the scope of our on-going work. Another model limitation is the idealizing assumption of surface area conservation, which is obviously violated in our experiments (Fig. 4). The area expansion observed often induces additional elastic responses of the membrane, which need to be properly included in an improved theory.

V.   CONCLUSION

In this work, we presented a study of vesicle deformation under strong DC electric fields. We systematically quantified the degree of deformation as a function of the field strength and the conductivity ratio. In particular, we studied large deformations in the prolate regime ($\gamma > 1$) with aspect ratios approaching 13 in extreme situations. We observe that the degree of deformation depends monotonically on the magnitude of the applied electric field. In addition, it also depends strongly on the conductivity ratio, exhibiting a positive correlation followed by a plateau. An estimate of the apparent vesicle surface area suggests significant expansion during pulsation, and reduction afterwards when the vesicles relaxed back to a spherical shape. Concurrently, the vesicle volume decreased throughout the process. These dynamic changes indicate membrane losses induced by electroporation. Indeed, the transmembrane potential exceeded the critical threshold for electroporation for most of the experiments performed.

We have developed a mechanistic model to predict the deformation process, and to interpret the experimental results. The model extends from that by Hyuga *et al.* [17]. In contrast to all previous theories which are limited to the linear, small-deformation regime, the current model is able to predict large membrane electrodeformations. A comparison between the model results and the experimental data reveals both agreement and discrepancy. Specifically, the dependence of the aspect ratio on the conductivity ratio and the applied field strength is well-captured by the model, and the data trends can be explained by the behavior of the driving electrostatic force. On the other hand, the model predicts that the aspect ratio decreases along with an increasing vesicle diameter, whereas such trend is not observed in the experiments. This discrepancy points to the limitations of the current model, which can be possibly improved via the development of a more rigorous electrohydrodynamic theory.

APPENDIX. Coefficients used in Eqn. (20)

The coefficients K_0, , and Q_F appearing in Eqn. (20) are defined with the following expressions:

$$K_0 = -\frac{\pi \rho_m a_0^4 \tan\Theta}{4\sin^2\Theta(\cos\Theta\sin\Theta+\Theta)^4}[-\Theta^3(1+8\cos^4\Theta)+\Theta^2\cos\Theta\sin\Theta(6\cos^2\Theta-1)$$
$$+\Theta\cos^2\Theta\sin^2\Theta(1+4\cos^2\Theta)+\cos^3\Theta\sin^3\Theta(1-2\cos^2\Theta)], \tag{23}$$

23

$$Q_\mu = -\frac{2\mu a_0^4 \pi}{\cos\Theta\sin\Theta(\cos\Theta\sin\Theta+\Theta)^2}[\cos\Theta\sin\Theta(2\cos^2\Theta+1)-\Theta(4\cos^2\Theta-1)]$$

$$-\frac{4\mu a_0^4 \pi}{\sin\Theta(\cos\Theta\sin\Theta+\Theta)^4}[2\Theta^3\cos\Theta(2\cos^2\Theta+1)-\Theta^2\sin\Theta \qquad (24)$$

$$+2\Theta\cos\Theta(\cos^4\Theta-1)-\cos^2\Theta\sin^3\Theta],$$

$$Q_F = \pi\varepsilon E^2 B^2 a_0^3(\gamma^2-1)\left\{-\frac{4}{3}\sqrt{\frac{2\cos^3\Theta\sin\Theta}{(\cos\Theta\sin\Theta+\Theta)^3}}\right.$$

$$\left.-2\sqrt{\frac{2\cos^3\Theta}{\sin^5\Theta(\cos\Theta\sin\Theta+\Theta)^5}}[\sin\Theta-\operatorname{arctanh}(\sin\Theta)]\left[\Theta(2\cos^2\Theta+1)+\cos\Theta\sin\Theta\right]\right\}(25)$$

VI.   REFERENCES

[1]   J. Gehl, Acta Physiol. Scand. **177**, 437 (2003).
[2]   L. M. Mir *et al.*, P. Natl. Acad. Sci. USA **96**, 4262 (1999).
[3]   J. Teissié, M. Golzio, and M. P. Rols, Biochim. Biophys. Acta **1724**, 270 (2005).
[4]   J. M. Escoffre *et al.*, Mol. Biotechnol. **41**, 286 (2009).
[5]   M. Kummrow, and W. Helfrich, Phys. Rev. A **44**, 8356 (1991).
[6]   G. Niggemann, M. Kummrow, and W. Helfrich, J. Phys. II **5**, 413 (1995).
[7]   P. K. Wong, W. Tan, and C. M. Ho, *Biomech. J.* **38**, 529 (2005).
[8]   T. R. Gowrishankar, and J. C. Weaver, Biochem. Biophys. Res. Commun. **349**, 643 (2006).
[9]   K. Kinosita, Jr *et al.*, Biophys. J. **53**, 1015 (1988).
[10]   W. Krassowska, and P. D. Filev, Biophys. J. **92**, 404 (2007).
[11]   J. Li, and H. Lin, Bioelectrochemistry   (2010, in Review).
[12]   G. Pucihar *et al.*, Biophys. J. **95**, 2837 (2008).
[13]   D. P. Tieleman, BMC Biochem. **5**, 10 (2004).
[14]   P. T. Vernier *et al.*, J. Am. Chem. Soc. **128**, 6288 (2006).
[15]   B. Gabriel, and J. Teissie, Biophys. J. **76**, 2158 (1999).
[16]   M. Winterhalter, and W. Helfrich, J. Colloid. Interf. Sci. **122**, 583 (1988).
[17]   H. Hyuga, K. Kinosita, Jr, and N. Wakabayashi, Jpn. J. Appl. Phys. **30**, 1141 (1991).
[18]   H. Hyuga, K. Kinosita, Jr, and N. Wakabayashi, Jpn. J. Appl. Phys. **30**, 1333 (1991).
[19]   D. Needham, and R. M. Hochmuth, Biophys. J. **55**, 1001 (1989).
[20]   S. Aranda *et al.*, Biophys. J. **95**, L19 (2008).
[21]   R. Dimova *et al.*, J. Phys.: Condens. Matter **18**, S1151 (2006).
[22]   R. Dimova *et al.*, Soft Matter **5**, 3201 (2009).
[23]   R. Dimova *et al.*, Soft Matter **3**, 817 (2007).
[24]   S. Kakorin, T. Liese, and E. Neumann, J. Phys. Chem. B. **107**, 10243 (2003).
[25]   S. Kakorin, E. Redeker, and E. Neumann, Eur. Biophys. J. **27**, 43 (1998).
[26]   K. A. Riske, and R. Dimova, Biophys. J. **88**, 1143 (2005).
[27]   K. A. Riske, and R. Dimova, Biophys. J. **91**, 1778 (2006).
[28]   P. M. Vlahovska *et al.*, Biophys. J. **96**, 4789 (2009).
[29]   M. I. Angelova, and D. S. Dimitrov, Faraday Discuss. **81**, 303 (1986).
[30]   T. Portet *et al.*, Biophys. J. **96**, 4109 (2009).
[31]   G. Stulen, Biochim. Biophys. Acta. **640**, 621 (1981).
[32]   H. Hyuga, K. Kinosita Jr, and N. Wakabayashi, Bioelectrochem. Bioenerg. **32**, 15 (1993).
[33]   N. Bentenitis, and S. Krause, Langmuir **21**, 6194 (2005).